Distributed System of Mobile Passive Tensegrity Structures

Kelly Y. Wang[1*], Adam V. Duran[1], Christine A. Gebara[1], Nicholas M. Saltarelli[2], Allison M. Ayad[2]

Jet Propulsion Laboratory, Pasadena, CA, 91109, United States

Abstract

A study on the application of spherical tensegrity structures to a passively mobile tumbleweed-like concept was developed and tested. Parameterized sizing tools were developed to understand environmental and geometrical sensitivities and maintain the ability to apply the concept to various environments. The sensitivity studies were then used to inform the design, and then a prototype model for an Earth environment was built to correlate the sizing tool outputs with experimental data. This prototype underwent testing in order to understand performance of the structure in more controlled (wind tunnel testing) environments and more realistic (field testing) environments. This paper will describe the design derivation and sensitivity studies performed along with the test results of the prototype structure.

Nomenclature

C_D	=	coefficient of drag
F_D	=	drag force
m	=	meters
M_t	=	tensegrity mass
β	=	configuration angle
ρ	=	density
R	=	radius
s	=	second
θ	=	inclination angle
U_∞	=	wind speed
W	=	weight

I. Introduction

Classic tensegrity geometries utilize a set of compression members held together by a series of continuous tension members, thus creating a geometry that does not put any of its members into bending. Due to this configuration, tensegrity structures can obtain high stiffness-to-mass ratios, not only offering mass benefits but also creating an impact-tolerant system [ref. 1]. In addition to its impact robustness, tensegrity systems contain redundancy in its features and can stow efficiently [ref. 2]. Tensegrity structures offer many benefits and have the potential to open up new mission architectures to explore more demanding terrains.

Meanwhile, the concept of a tumbleweed mission architecture is compelling because it takes advantage of its surrounding environment for mobility, thereby reducing vehicle complexity. This concept has been pursued in the past with inflatable designs, particularly at NASA Langley Research Center [ref. 3]; however, tensegrity structures

[1] Mechanical Engineer, NASA Jet Propulsion Laboratory, California Institute of Technology. *Corresponding author, Kelly.Y.Wang@jpl.nasa.gov

[2] Engineering Undergraduate Student, NASA Jet Propulsion Laboratory, California Institute of Technology.

bring the added advantage of not having to rely on inflatables, which contain single point failures. The previous research developed with an inflatable application will be used as a reference in the design approach and parameter assumptions in this paper.

This paper looks at the intersection of these two concepts, better understanding the feasibility by using the Martian environment as a case study. Section II delves into the sizing approach and sensitivity studies, concluding with how the findings were incorporated into the design, while Section III focuses on the testing performed to validate the model's parameter assumptions and the overall concept feasibility.

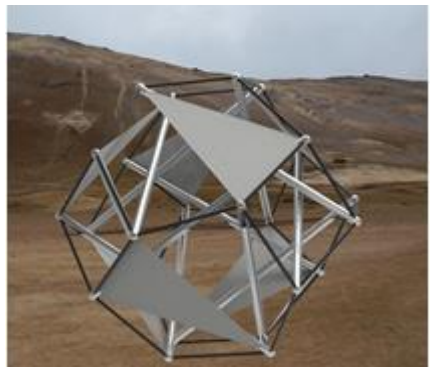

Fig. 1 Tensegrity structure with conceptual aero surface design for passive locomotion.

II. Design Approach

A. Governing Equation

Following the approach of the quasi-static analysis in previous work at NASA Langley Research Center [ref. 3], the sizing of the tensegrity structure was done by equating the sum of the moments to the drag force. The structure was assumed to be on an incline θ as shown in Figure 1. Here, the forces acting on the body are the drag force, the weight, and the normal force, where friction is neglected. For simplicity, the free stream velocity is assumed to always act parallel to the slope of the ground. The rolling resistance is accounted for by offsetting the normal force by l_0. Although the structure is assumed to be completely rigid, the perpendicular distance between the surface and the center of mass is not equal to the radius of the structure. This is due to the fact that the structure has distinct discreet points (i.e. not continuous) at which it makes contact with the surface. This offset is related to the offsetting normal force by the angle β. Summing the forces in the y-direction and taking the moment about point O, the relation at equilibrium is

$$F_D = Wsin(\theta) + Wcos(\theta)\tan(\beta) \tag{1}$$

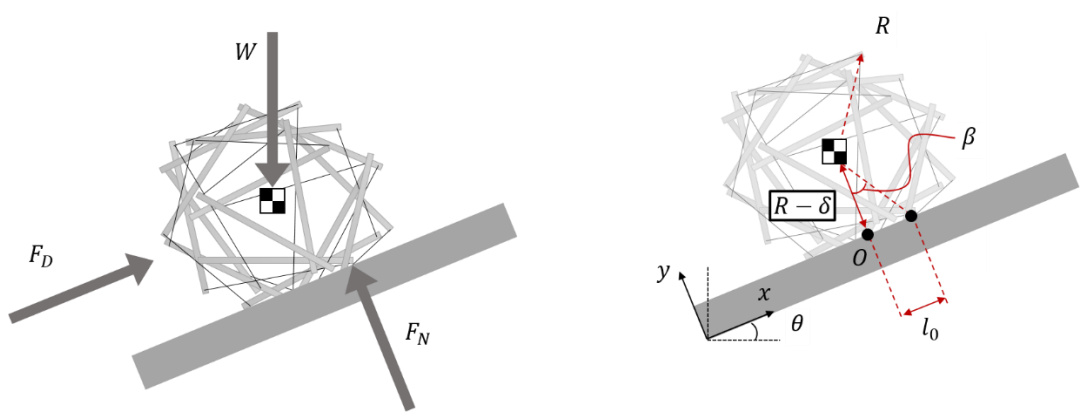

Fig. 2 Free body diagram and geometry of Tumbleweed structure

where F_D is the force needed to maintain equilibrium; exceeding this force is required for mobility. Using the drag force equation $F_D = 0.5\, C_D\, A_i\, \rho\, U_\infty^2$, and the relations $W = M_t g$ and $A = \pi R^2$, the governing equation is expressed as

$$sin(\theta) + cos(\theta)\tan(\beta) = \frac{\pi\, \rho\, U_\infty^2}{2g}\left(\frac{C_D R^2}{M_t}\right) \tag{2}$$

Equation 2 is arranged such that the angle θ is a function of the environmental and tensegrity design variables. However, in this work, it is assumed that the environmental variables, ρ, g, U_∞ are constant, with the design variables grouped separately; i.e. $\theta \equiv f(C_D, R, M_t, \beta)$. Although these design variables are assumed to be independent, it can be argued that they are related, or in the case of the coefficient of drag, they too are a function of the environment ($C_D \equiv f(R_e)$). For example, it is intuitive that if the radius R of the structure increases, so too will the mass, M_t implying that $\theta \equiv f(R^n)$ where $0 < n \leq 2$. These relationships are highly configuration dependent and are examined in the following sections. For simplicity, these variables are assumed to be independent in this section. By inspection Equation 2 is highly nonlinear, however, insight can be gained by assuming the limiting case where $\tan(\beta) = 0$. The limiting case implies that the structure has no rolling resistance, as the offset is zero, and yields an inverse sine function. Here we set the right hand of the governing equation to the variable χ.

$$sin(\theta) + cos(\theta)\tan(\beta) = \chi \tag{3}$$

For $\theta \to 90°$, $\chi \to 1$. Assuming that there is no control over the environmental variables, it is clear that the objective is to maximize the coefficient of drag, maximize the radius of the structure and minimize the mass. Of course, as previously noted, the mass and the radius are related. However, this gives a clear design objective and intuitively makes sense, especially with environments with low dynamic pressures (e.g. Mars); a design that is large, lightweight and creates sufficient drag to roll. The situation becomes much more complicated when the rolling resistance term β is reintroduced. Solving Equation 3 for the incline angle θ yields the inverse tangent function shown in Equation 4. This relationship is plotted on Figure 3 below.

$$\theta = 2\tan^{-1}\left(\frac{1-\sqrt{1-\chi^2+\tan(\beta)^2}}{\chi+\tan(\beta)}\right) \tag{4}$$

The logarithmic plot shows the inclination angle θ as a function of the parameter χ. Recall the variable χ represents the right hand side of the governing equation (Eq. 2). Each line represents a different angle β ranging from zero to forty degrees. The upper bound ($\beta = 0°$) is represented by the upper most black line. At first inspection it is clear that the rolling resistance angle greatly influences the performance of the structure; a higher β angle greatly reduces the angle at which the structure can climb. For example, for $\chi = 0.5$ the upper bound is able to achieve a slope of $\theta = 30°$. For the same value of χ, a structure with a $\beta = 10°$ (grey triangle) and a $\beta = 20°$ (purple dot dashed) are only able to achieve a slope of $\theta = 20°,\ 8.5°$ respectively. Furthermore, structures with increased rolling resistance angles ($\beta = 30°, 40°$), do not register on the plot and thus do not move. In order to climb the same incline as the $\beta = 20°$ structure, the $\beta = 40°$ (red boxed) must double its χ.

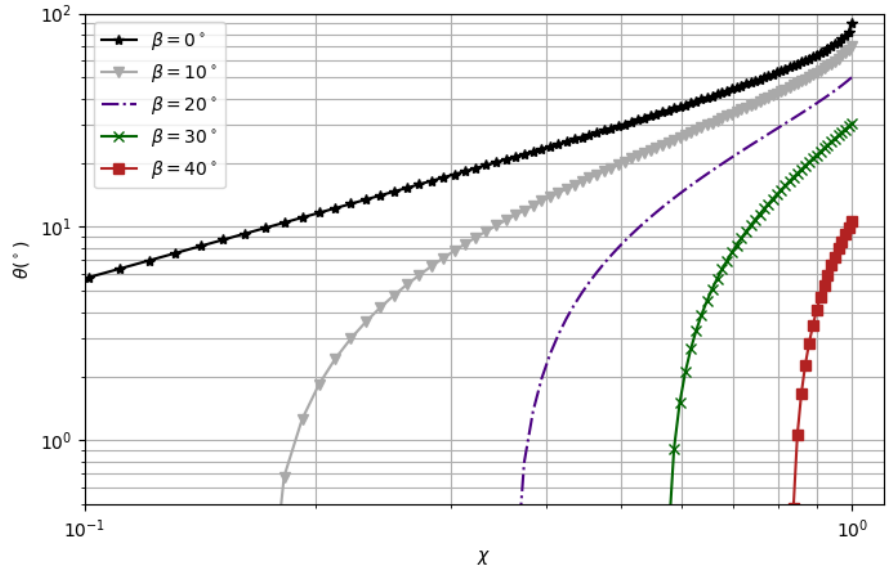

Fig. 3 Plot of inclination angle θ as a function of parameter χ.

To further investigate the behavior of Figure 3, a sensitivity analysis was performed by perturbing both χ and β near a nominal point. Results for this study are shown on Table 1. Three studies are shown where each has a nominal χ_0 and β_0 value. These values are then perturbed by 10% and the corresponding incline value is reported along with the ratio with the nominal incline value θ_0. Study 1 starts with a $\chi_0 = 0.45$ and a $\beta_0 = 20°$ corresponding to a $\theta_0 = 5.0°$. By decreasing the rolling resistance angle by 10%, the performance to when compared to nominal increases by 46%. However, if the rolling resistance angle β remains fixed and the parameter χ is increased by 10% the performance increases by 54%. This shows that although the angle β plays a large role in determining the performance of a structure, the inclination angle is more sensitive to the parameter χ. Study 2 increases the nominal parameter $\chi_0 = 0.90$ but holds $\beta_0 = 20°$. A similar trend is found to that of Study 1 in that the inclination angle is more sensitive to the parameter χ. However, comparing Study 1 to Study 2 it is observed that the inclination angle is overall less sensitive to the perturbations in general for higher values of χ. The maximum benefit was a 30% increase to performance, while Study 1 yielded 54%. Finally Study 3 holds the nominal parameter $\chi_0 = 0.45$ but decreases $\beta_0 = 10°$. Study 3 shows that by decreasing the rolling resistance angle, Equation 3 becomes less sensitive in general to both χ and β. These results are confirmed by inspection of the slopes in Figure 3.

			θ (°)	θ/θ_0
Study 1	$\chi_0 = 0.45$	$\beta_0 = 20°$	5.0	1.00
	$\chi = \chi_0$	$\beta = 0.9\beta_0$	7.3	1.46
	$\chi = 1.1\chi_0$	$\beta = \beta_0$	7.7	1.54
Study 2	$\chi_0 = 0.90$	$\beta_0 = 20°$	37.0	1.00
	$\chi = \chi_0$	$\beta = 0.9\beta_0$	40.9	1.10
	$\chi = 1.1\chi_0$	$\beta = \beta_0$	48.5	1.30
Study 3	$\chi_0 = 0.45$	$\beta_0 = 10°$	6.0	1.00
	$\chi = \chi_0$	$\beta = 0.9\beta_0$	17.4	1.08
	$\chi = 1.1\chi_0$	$\beta = \beta_0$	19.2	1.19

Table. 1 Study on the sensitivity of geometric parameters.

In summary, the governing equation was solved for a performance metric of the inclination angle θ. This highly nonlinear equation is sensitive to the parameter χ and the rolling resistance angle β. To maximize performance, the parameter χ must increase while the angle β must decrease. Following the assumption that the environmental variables, ρ, g, U_∞ are constant χ can be thought of as a unit less scaled specific area; i.e. $\chi \propto C_D R^2/m$. These variables are highly configuration dependent and are investigated in the following sections with respect to tensegrity structures.

B. Tensegrity Structure

Tensegrity structures are typically composed of three components: bars, cables and joints. For this application, sails augment the structure and are conservatively assumed to act as the only aero surface on the structure; i.e. the bars, cables and nodes do not create drag. The environmental variables used in this case study are $U_\infty = 10\mathrm{m/s}$, gravity $g = 3.69\ \mathrm{m/s^2}$ and a density $\rho = 0.0155\ \mathrm{kg/m^3}$. Thus the term outside the parenthesis in Equation 2 is $0.66\ kg/m^2$. This implies $\chi = 0.66 C_D R^2/M_t$, where M_t is the total mass of all components. For this work, a representative payload mass of $1.8\ kg$ is assumed to be supported at the center of the structure.

In tensegrity structures, the bars act as compression members. In a potential mission architecture, the tensegrity structure would have to survive multiple load cases such as launch, thermal environments, radiation environments, deployment and impact. Once the structure is deployed it could potentially fall off a cliff; another structurally dangerous environment. However, the scope of this work focuses on the mobility of the structure and, as described in the previous section, the maximization of θ through χ and β. In this work, the load experienced by these scenarios is neglected. Thus the primary objective is to decrease mass, M_t, and decrease the rolling resistance through β. Again the bars do not act as aero surfaces, however, there are implications for the coefficient of drag C_D. The total mass of the structure is described as the sum of the mass of all components. The contributions from the bars are as follows

$$M_b = \rho_b A_b C_b R \eta_b \tag{5}$$

where ρ_b is the density of the bar material, A_b is the cross sectional area of the bar, C_b is a geometry-specific scale factor relating the structure radius R to the bar length, and η_b is the number of bars in the structure. In this work, two tensegrity architectures were examined; the 12-bar and 30-bar structures as shown in Figure 4 below. Assuming the same cross sectional area, material and radius R, the mass ratio between the two structures is $M_{12}/M_{30} = 12C_{12}/30C_{30}$=0.54 where, C_{12}= 0.92 and $C_{30} = 0.67$. Assuming a typical carbon composite tube ($\rho = 1700\ \mathrm{kg/m^3}$) with a $1mm$ thickness, outer radius of $2mm$, a tensegrity radius of $1.5m$, and a $C_D = 1$,the mass of the 12 bar structure is $M_{b,12} = 0.52kg$. Summing with the total mass yields $\chi_{12} = 0.66 C_D R^2/(1.8kg + M_b) = 0.64$. Scaling for the 30 bar structure yields $\chi_{30} = 0.53$ and $M_{b,30} = 0.96kg$, showing the detrimental effects of almost doubling the structure mass. It is clear from this particular comparison that in terms of mass, the 12-bar structure is superior. Furthermore, by adding more bars, there is an additional increase in mass due to the quantity of cables (36 to 90) and the nodes (24 to 60) needed for the structure. However, there are advantages to having the 30-bar design in the context of C_D and β.

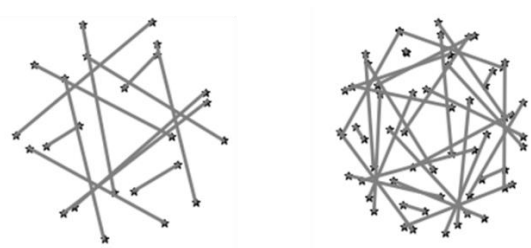

Fig. 4: 12 bar structure (left) and 30 bar structure (right).

One clear advantage for the 30-bar geometry has to do with sail configuration options. For the 12-bar structure, there are 44 unique surfaces that are defined by the outer points. Meanwhile, the 30-bar structure contains 122 such surfaces as shown in Figure 5. In trying to increase the coefficient of drag, the 30-bar structure provides more opportunities to maximize this value. Furthermore, the rolling resistance angle to the 12-bar structure is greater than the 30-bar structure, due to the fact that there are more discrete contact points for the 30-bar structure (60 vs 24). For a 12-bar structure, $\beta_{12} = 42°$ while the 30 bar structure yields $\beta_{30} = 22°$. It is clear from the given parameters for the

12-bar structure ($\chi_{12} = 0.64$, $\beta_{12} = 42°$) that no solution exists when examining the plot on Figure 3. However, for the 30-bar structure ($\chi_{30} = 0.52$, $\beta_{30} = 22°$), the inclination angle is $\theta = 7.4°$. Thus the 30-bar architecture was baselined for this study.

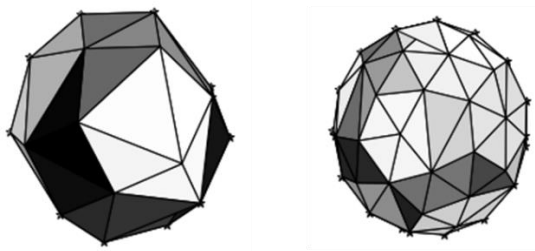

Fig. 5: 12 bar unique surfaces (left) and 30 bar unique surfaces (right).

Next, the joints were investigated. Tensegrity joints are typically moment releasing and act as a junction between the cables and bars. In this work, a basic tensegrity joint was compared to a modified joint. These joints are shown in Figure 6 below. Both joints are similar in that the smaller holes are the cable attachment points and the singular large hole accommodated the bar. The advantage to the common joint is that is simple in geometry and has less volume than the modified joint. However, the modified joint was designed to further decrease the rolling resistance of the structure. The bottom surface of the joint was designed to make contact with the surface, and the angle between the "blade" feature and the main structure was designed to reduce the angle β. This modification would allow moments to be carried through the joint, no longer putting the bar in pure compression. While this may lead to a discussion on the class and type of tensegrity, since classical tensegrity structures do not allow transfer of moment through the nodal joints, for the application discussed in this paper, the tensegrity structure does not undergo significant flexing and moments carried through the joint do not affect the sizing or form of the structure. In both the basic and modified joint design, the cables do not intersect the compression member at the same exact point due to ease of manufacturing. This induces in a small moment, since the cables are slightly offset from each other at the end of each compression member. However, in terms of performance, the main implication for the joints is mass and rolling resistance. The basic joint still corresponds to a $\beta = 22°$. Assuming the same dimensions for the bar and structure as before, and a density of PLA ($\rho = 1240\ \mathrm{kg/m^3}$), the mass of 60 basic joints is $0.12kg$ while the mass of 60 modified joints is $0.30kg$. Including these mass contributions to the total mass of the system and solving $\chi = 0.66C_D R^2/(1.8kg + 0.96kg + M_j)$ yields $\chi = 0.52$ and $\chi = 0.48$ for the basic and modified joint respectively. With the incorporation of the joint mass fidelity, the basic joint performance decreases from $\theta = 7.4°$ to $\theta = 6.8°$. However, because the modified joint reduces the rolling resistance angle to $\beta = 13°$, the capability of the structure actually increases to $\theta = 14.8°$. The modified joint is therefore superior to the basic joint and is incorporated into this design.

Fig. 6 Simple tensegrity joint (left) and modified joint (right).

The final design challenge was to investigate sail implementation. Two design paradigms were considered; aero surfaces external to the structure and aero surfaces internal to the structure (using three orthogonal planes). In the governing equation, these surfaces influence both the coefficient of drag C_D and the mass of the structure. The two design paradigms are shown in Figure 7. External surfaces are advantageous in that there are 144 options in the design space. Having all surfaces attached would guarantee that no matter the angle at which the free stream velocity approaches, the structure will always have the full structure exposed to the incoming wind. Furthermore, these surfaces can be further tuned for the desired coefficient of drag, or surface coverage. In fact, this paradigm lends itself well to discreet optimization. One could imagine a solution with only a few surfaces that still allow the structure to be sufficiently exposed to the incoming wind. However, there are a few limitations to this design, the first being that the

coefficient of drag is unknown. For the limiting case of all 144 surfaces, the structure resembles a sphere with a known $C_D = 0.47$ and a mass scaling with $4\pi R^2$. Furthermore, these surfaces would be exposed to the outside environment where they could potentially be torn on rocks or other obstacles, similar to the previously studied inflatable technology. Finally this design would limit the field of view of potential science instruments embedded in the center of the structure. In contrast, the internal design uses 3-orthogonal planes as aero surfaces. These planes ideally intersect at the geometric center of the structure, allowing for visibility from the center and a mass scaling with $3\pi R^2$. The three orthogonal plane design, or box-kite design, has been studied in the past and has published values of $C_D = 1.1$ [ref. 4]. Additionally, the box-kite design is more robust than the external design in that the surfaces are not exposed to obstacles such as rocks. One limitation of the box-kite design is that it is not omnidirectional; although most orientations have sufficient coverage to the incoming wind, there exists an orientation where the exposed area to the free stream is less than area of the fully populated external design. Specifically, if the exposed area of the external surface is A_0 the exposed area of the box kite design, at the worst orientation, is $0.7A_0$. This influences the radius of the structure R in the governing equation by a factor of $\sqrt{0.7}$.

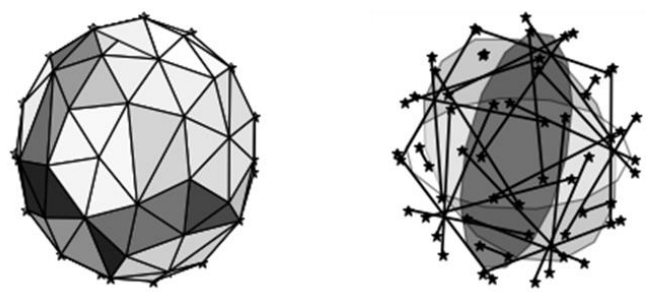

Fig. 7: External sail configuration (left) and internal sail configuration (right).

In terms of mass, the work assumed the lightweight UHMWPE Dyneema fabric with a mass per unit area of $0.017\ kg/m^2$ for the aero surfaces. The mass of the external configuration is calculated by taking the product of the surface area and mass per unit area; $(4\pi 1.5^2)(0.017) = 0.48kg$. Including this mass contribution to the total mass of the system and solving $\chi = 0.66C_D R^2/(1.8kg + 0.96kg + 0.30kg + 0.48kg)$ yields $\chi = 0.42$. However, this value assumes a coefficient of drag of unity. Scaling to a more realistic value yields a value of $\chi = 0.25$ dropping the performance of the structure to $\theta = 1.1°$. For the box kite configuration the mass is calculated as $(3\pi 1.5^2)(0.017) = 0.36\ kg$. Before calculating the mass of the system, the coefficient of drag is adjusted to $C_D = 1.1$ and the radius of the structure R is scaled by $\sqrt{0.7}$ as discussed earlier. Therefore, $\chi = 0.66C_D\left(\sqrt{0.7}R\right)^2/(1.8kg + 0.96kg + 0.30kg + 0.36kg) = 0.33$ corresponding to an inclination of $\theta = 5.8°$.

In summary, multiple design trades were considered when developing the tensegrity tumbleweed structure. It was found that the 30-bar structure with augmented nodes and internal aero surfaces provided the best mass, coefficient of drag and size benefits culminating in the final design shown in Figure 8. In the following section, this design approach was applied to Earth's environmental parameters and an Earth Analog Tensegrity (EAT) unit was built in order to verify the concept through testing.

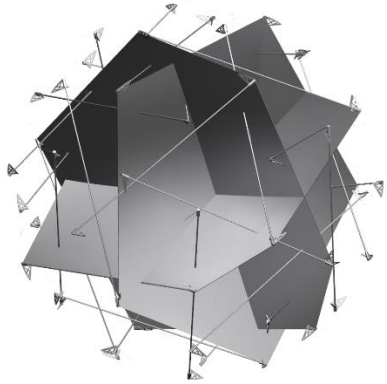

Fig. 8 Final 30-bar design with modified joints and internal sails

III. Testing and Verification

In order to correlate expected system performance with empirical data, testing was carried out in both a laboratory environment and in the field. The tensegrity unit was scaled using Earth's environmental variables (gravity $g = 9.81\ \mathrm{m/s^2}$ and density $\rho = 1.225\ \mathrm{kg/m^3}$) and lower wind speeds for field testing purposes ($U_\infty = 5\mathrm{m/s}$). With the incorporation of these environmental parameters into the governing equation, the test structure was determined to be 0.80m in diameter.

A. Wind Tunnel Testing

A series of tests done at the California Institute of Technology's Lucas Wind Tunnel were used to characterize the aerodynamic performance of the system in a sweep of different airspeeds and positions. There were two major test campaigns: the first focused on determining critical wind speeds at which the tensegrity began rolling and the second focused on calculating drag coefficient values.

The first set of testing focused on determining the wind speeds required to induce enough moment to overcome the rolling resistance of the tensegrity structure. The wind tunnel test setup for this first set of tests is shown in Figure 9. Out of the nine configurations tested, the highest required wind speed to roll the tensegrity on smooth, flat ground was 4.55 m/s. Given that the prototype was sized for a velocity of 5 m/s, there is a slight conservatism in the sizing method.

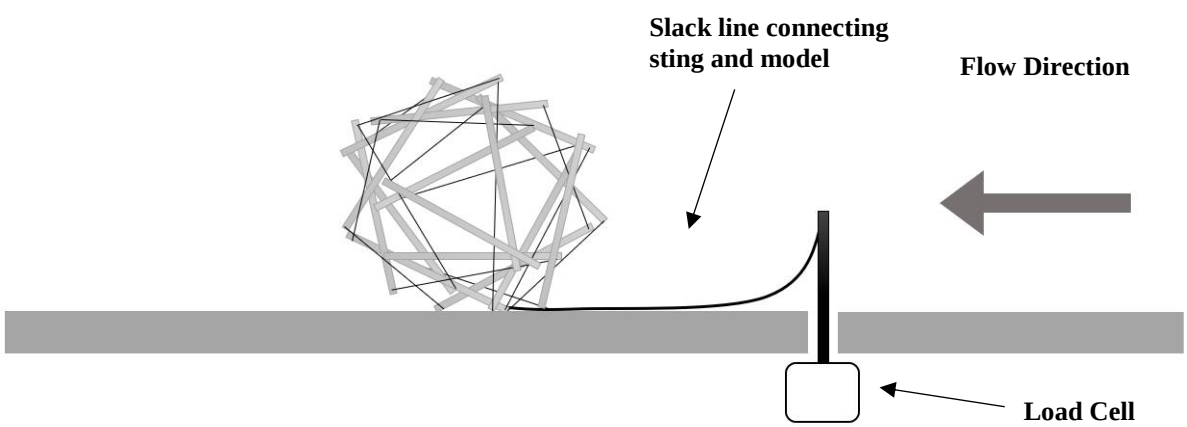

Figure 9: Side View of wind tunnel setup for rolling tests.

Figure 10: Image of wind tunnel set up (photo taken from flow direction)

The second set of testing resulted in better definition of the drag coefficient values. We gathered drag coefficient values of nine configurations at a sweep of seventeen wind speeds ranging from 2 m/s to 10 m/s, each test with an interval of half a meter per second. The nine configurations ran were selected in order to orient the tensegrity in such a way that the minimum drag area was facing the direction of the wind. Figure 11 displays the test setup with the tensegrity structure attached.

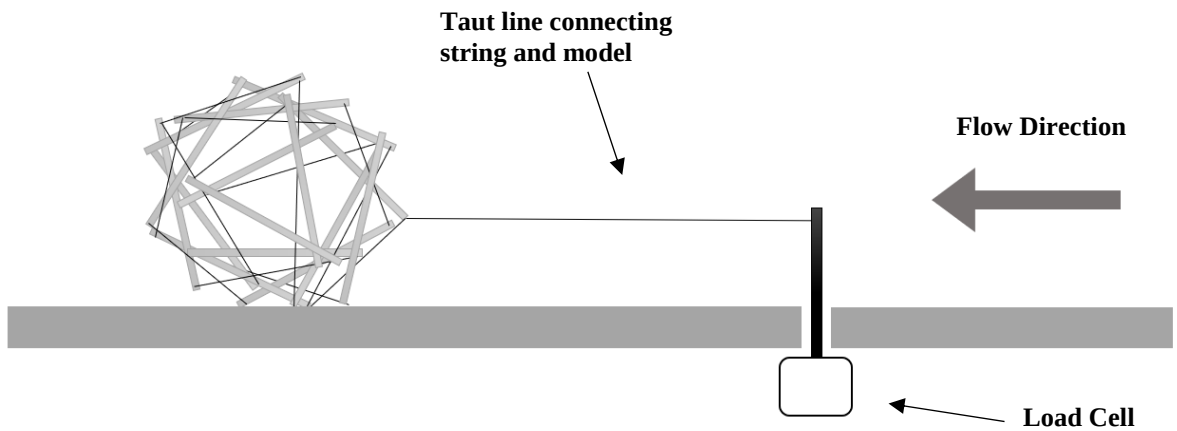

Figure 11: Side View of wind tunnel setup for drag coefficient tests

There were two main trends identified in these tests: the first was the transition of the flow from laminar to turbulent, and the second was a readjustment of the model. The transition from laminar to turbulent flow can be seen in Figure 12, between airspeeds of 2 m/s to 6 m/s, as the inertial forces overcome the viscous forces acting in the fluid. Once flow exceeds 6 m/s, the primary contributor to drag comes from the inertial forces, corresponding with the coefficient of drag stabilization. However, two effects from the setup can be seen in this figure: the first occurring at 6.5 m/s and the second at roughly 8-9 m/s. It can be concluded that the first occurred because the model had a large enough coupled moment created by the opposing drag force and the tension to reorient itself, as shown in the first and second panels in Figure 13. The second minor blimp corresponded to the model lifting itself off the ground due to the vertical component of the tension, as seen in the third panel of Figure 13.

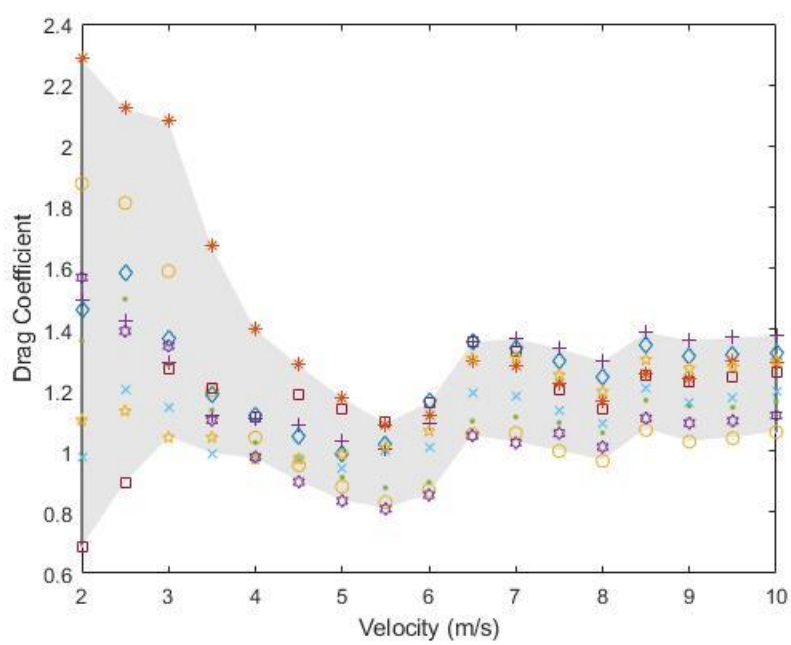

Figure 12: Drag coefficient vs air velocity

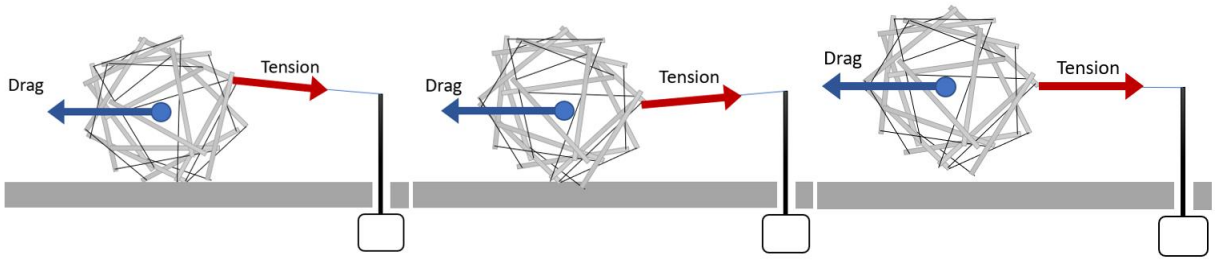

Figure 13: Three stages during wind tunnel testing.

In this test set up, the load cell was attached by a string located in front of the test subject in order to add a taut line for rolling tests. This mounting method introduced alignment biases in both pitch and yaw due to the model trying to find its most statically stable configuration. For future testing, this set up could be improved so that the model is placed in an orientation where the line of action of the drag and tension are collinear, thereby eliminating the moments or lifting that was observed during this testing. In the end, the data showed the lowest drag coefficient was 1.05, consistent with the assumptions made in the model ($C_D = 1.1$ was assumed).

B. Field Testing

While wind tunnel testing was meant to assess the aerodynamic performance of the system, field testing was carried out to assess the performance of the system in a realistic environment. Figure 14 displays an image of the type of terrain that was selected for field testing. A half day of field testing was carried out in the area near Palmdale, California.

Figure 14: Images displaying two environments where field testing was conducted. Sandy river bed (left) and desert with dead brush (right).

During field testing, the system was outfitted with a GoPro Fusion camera suspended in the center of the structure. The GoPro Fusion collects 360-degree footage using two separate sensors. During post processing of video footage, the imagery is stitched together and stabilized using stored accelerometer data. This camera weighs 226 grams, which is significantly less massive than the expected payload of the system. This mass is also significantly lower than the mass of the payload used for wind tunnel testing. This decrease in mass was intentional to capture video footage that would be representative of what may be possible during a Martian mission. Figure 15 displays the field of view from the center of the structure.

Figure 15: An example of 360 video capture from a camera suspended within the center of the structure. The pink in the image is the edge of the camera mount.

During field-testing, the system successfully carried out the following tasks:

- Rolling uphill on both a dirt road and obstructed desert terrain
- Becoming stuck on an obstacle, and then becoming free after a short time interval
- Becoming airborne after gaining speed and then rolling over an obstacle

Numerous observations came from field testing. Design of the nodes is important to avoid becoming entangled with brush. Figure 16 displays a branch that caused the structure to become immobile. It is safe to assume no branches would be present on Mars, however, the system nodes will need to be designed to be robust to sharp rocks and other obstacles. These accommodations would not change the fundamental system design. Further, the system performed better than expected in inconsistent wind. Low, inconsistent wind (less than 3 m/s) was still able to create meaningful motion of the system. Finally, the system was sometimes able to quickly escape obstacles after becoming stuck. The escape often correlated with an increase in wind speed or a change in direction.

Figure 16: Image of brush becoming entangled with structure node.

In the future, extensive field testing will be needed to improve the understanding of the how the system performs in the field. Due to the time constraints of the campaign, this field testing was carried out over short time intervals. If the system was idle, or appeared stuck on an obstacle, field testing was reset after about a minute of no movement. Field testing did not focus on system performance in a local minima or 'crater' like topography. However, no issues were observed with the system getting stuck in small sand deformations up to a quarter of the system radius. Further, as mentioned, this field testing did not include the full payload mass of the system. This would ideally be incorporated into future campaigns. Additional testing with a prototype of the system payload would allow for simulated science data to be collected. Field testing of various sail and node configurations may provide more insight into whether the

small design changes may improve the system's ability to avoid obstacles. The system design was based on rolling on a flat surface. Considering rough terrain may change the design of the structure elements that interact with the ground.

IV. Summary and Conclusions

In conclusion, the concept of using a tensegrity structure in a tumbleweed application was studied through a sensitivity study and subsequent validation testing. The Martian environment was chosen as a case study in order to quantify the sizing sensitivities for a realistic use case. This study indicates that a tensegrity tumbleweed of 1.5m diameter would be able to roll in a Martian environment up an incline of 6°, assuming 10 m/s wind speeds. The parameterized tools developed give us the capability to size other structures for different environment, configuration and performance variables. Further, both the wind tunnel testing and field testing observations confirm that this sizing method is conservative. As mentioned previously, this conservatism could be better quantified through further testing and parameter refinements.

While this research focuses on a purely passive architecture, it can serve as a solid foundation for various other mission concepts. Simple control systems could potentially be incorporated to control *when* or *where* the system moves. For example, if science instruments need to stay stationary to take a sample or measurement, the tumbleweed could reduce its size to stay in one location and then increase its size once the measurement has taken place. Additional features can also be incorporated to control the direction of movement if necessary.

Acknowledgments

This research was carried out at the Jet Propulsion Laboratory, California Institute of Technology under a contract with the National Aeronautics and Space Administration. The authors would like to thank the Offices of the Chief Scientist and Chief Technologist for supporting this work under the R&TD program. The authors would also like to acknowledge David Jeon for his assistance at the Caltech wind tunnel facility as well as our project advisors: Courtney Duncan, Kalind Carpenter, S. Case Bradford, Luther Beegle, Leslie Tamppari, and Ioannis Mikellides.

References

[1] Rimoli, J. "On the Impact Tolerance of Tensegrity-based Planetary Landers" AIAA SciTech Forum, 2016. doi: 10.2514/6.2016-1511

[2] Skelton, R. E. and de Oliveira, M.C. *Tensegrity Systems, Volume 1*. Springer, 2009.

[3] Antol, J., Calhoun, P., Flick, J., Hajos, G., Kolacinski, R., Minton, D., Owens, R., and Parker, J., "Low Cost Mars Surface Exploration: The Mars Tumbleweed," NASA TM-2003-212411, August 2003.

[4] Antol, J., Harris S.B., Hajos G.A., and Strickland, C.V., "Wind Tunnel Tests of Evolved Mars Tumbleweed Concepts," AIAA Paper 2006-0069, January 2006.

© 2019. California Institute of Technology. Government sponsorship acknowledged.